Modeling the photocatalytic oxidation of carboxylic acids on aqueous TiO_2 suspensions and on immobilized TiO_2-chitosan thin films in different reactor geometries irradiated by UVA or UVC light sources

Ivana Grčić[1,*], Natalija Koprivanac[2] and Gianluca Li Puma*[3]

[1]Faculty of Geotechnical Engineering, University of Zagreb, Hallerova aleja 7, HR-42000, Varaždin, Croatia

[2]Faculty of Chemical Engineering and Technology, University of Zagreb, Marulićev Trg 19, HR-10000, Zagreb, Croatia

[2]Environmental Nanocatalysis & Photoreaction Engineering, Department of Chemical Engineering, Loughborough University, Loughborough, LE11 3TU, United Kingdom

* Corresponding authors: I. Grčić (igrcic@gfv.hr) and G. Li Puma (g.lipuma@lboro.ac.uk)

Abstract

Photocatalytic reactor models incorporating radiation transport parameters and intrinsic kinetic parameters of photocatalytic decomposition of single-compound and mixtures of oxalic (OA) and formic acid (FA), in both slurry suspensions and immobilized photocatalytic thin films, were validated in two well-mixed annular photoreactors geometries irradiated with either UVA or UVC radiation. The six-flux absorption scattering model (SFM) predicted the radiation field in a titanium dioxide (TiO_2 P25) catalyst suspension, the local volumetric rate of photon absorption (LVRPA) at each point of the reactor and, after volumetric integration, the lumped VRPA. The model combining the lumped VRPA, the kinetics models describing the adsorption and photocatalytic decomposition of OA and FA and the material balance of the reacting species was fitted to the experimental results of photocatalytic decomposition of OA and FO in a slurry TiO_2 suspension, to determine the OA and FA intrinsic reaction kinetics parameters. Such intrinsic parameters were then used with the average surface rate of photon absorption (SRPA) to model and predict the photocatalytic oxidation of OA and FA on non-porous TiO_2–chitosan films immobilized on glass plates immersed in the photoreactor. The models for both slurry suspensions and immobilized photocatalysts predicted the degradation and mineralization of OA and FA and of a mixture of them under diverse experimental conditions. This study demonstrates a systematic methodology for determining intrinsic reaction kinetics rate parameters of water contaminants that can also be used to represent the photocatalytic oxidation of such contaminants in irradiated slurries and in immobilized photocatalytic thin films and in any photoreactor geometry.

Keywords: Semiconductor photocatalysis; Supported catalyst; Modelling; Water pollutant; Advanced oxidation processes

1. Introduction

Carboxylic acids, such as oxalic acid (OA), formic acid (FA) and short-chain carboxylic acids are common species in various industrial wastewater and natural waters. These compounds often are the products of the mineralization of aromatic compounds [1] by oxidation processes [2]. Among different types of industrial wastewater, petrochemical plants wastewater often contains high loadings of formic acid, which is challenging to remove [3]. Advanced oxidation technologies which are based on the production of highly reactive radical species (e.g., $OH^{\bullet}$) have shown many advantages for the treatment of such type of wastewater over conventional treatment methods [4-7]. Specifically, TiO_2 photocatalysis has been successfully applied for the treatment of oxalic, formic, gallic and other aliphatic and aromatic carboxylic acids in wastewater, due to strong chemisorption of these species on the TiO_2 surface and photocatalytic oxidation [8-12].

The removal of contaminant species by TiO_2 photocatalysis requires the effective irradiation of the TiO_2 catalyst, which can be either in an aqueous slurry suspension or immobilized onto a supporting substrate [13, 14]. In general, suspension or slurry type reactors provide more effective treatment of water contaminants than immobilized systems due to larger irradiated catalyst surface area and higher rate of mass transfer of reactants towards the catalyst surface [15]. However, a catalyst recovery stage involving microfiltration may be required to recover and reuse the catalyst. This process may add to the capital and operating costs of the water treatment process [16]. Alternatively, the TiO_2 may be immobilized onto an inexpensive supporting substrate, such as silica [17], as a thin film to ensure that the light can reach the entire layer of the supported photocatalyst [16,18,19]. Such configuration, however, reduces the total surface area of catalyst irradiated with light and the transport of reactants to the catalytic surface may be limited by mass transfer, which results in a reduction of the contaminant oxidation efficiency in most immobilized photocatalytic systems [18,19]. In

general, no clear answers can be gathered from the literature, since the process of choice often requires further engineering considerations, including scale-up and a process economics analysis [20].

The initial step in a semiconductor photocatalytic reaction mechanism involves the absorption of photons that have energy higher than the band-gap of the semiconductor and this process results in the generation of electron-hole pairs in the bulk of the catalyst. The photogenerated charges may then either recombine in an energy dissipating process or may migrate to the surface of the catalyst, giving place to interfacial charge transfer to the adsorbed species. The oxidation process can then proceed via attack by the •OH radicals generated upon hole trapping of OH^- or adsorbed water molecules, by direct hole transfer (h+) to an adsorbed pollutant or by attack by the radical oxidative species produced through the reductive pathway over the semiconductor. The most up-to-date findings suggest that the overall reaction rate of OA photodegradation can be described as a combination of two parallel pathways due to simultaneous occurrence of monodentate and bidentate surface complexes. The latter resulted in the observation of two kinetic regimes: a faster first order kinetics associated with hole trapping via OH^- and a slower square root dependence on the OA concentration due to direct hole trapping by the adsorbed species (half-order kinetics) [21,22].

Recently, a comprehensive kinetic model for the adsorption and photodecomposition of the model contaminant, OA on TiO_2 aqueous suspensions was combined with a validated radiation model (six-flux absorption scattering model (SFM)) to predict the photocatalytic oxidation of OA in two annular photoreactors operated with slurry photocatalyst suspensions [11]. The model fitted the experimental data obtained in photoreactors with different geometries, optical thicknesses and operating hydrodynamic regimes (turbulent batch mode and laminar flow through recirculation mode). This modeling methodology opens the possibility for determining meaningful intrinsic reaction rate constants of photocatalytic

degradation of water contaminants, which are independent of radiation field, hydrodynamic conditions, and reactor geometry. However, the determination of the oxidation the water contaminants on immobilized photocatalytic thin films using such kinetics parameters or parameters determined in advance using slurry photocatalytic reactors are scarcely reported in literature. Such studies are important for the translation of key design kinetics parameters for the design of photocatalytic water treatment systems utilizing suspended or immobilized photocatalysts.

In this study, the photocatalytic oxidation of single-compound and mixtures of two common carboxylic acids (OA and FA) catalyzed by either suspended TiO_2 or immobilized TiO_2 thin films was investigated in two batch photoreactors under different irradiation conditions (UVA or UVC). A comprehensive kinetic model describing the adsorption and photocatalytic decomposition of OA and a Langmuir-Hinshelwood model for FA were combined with the SFM, applied to a catalyst suspension, and with the material balance of the reacting species, to determine intrinsic reaction kinetics rate parameters for OA and FA. Such intrinsic reaction kinetic parameters determined from a slurry reactor configuration were then used to model the photocatalytic oxidation of OA and FA on TiO_2–chitosan films [23] immobilized on glass plates irradiated by different light sources (Fig. 1). Overall, this study demonstrates a systematic methodology for determining intrinsic reaction kinetics rate parameters of water contaminants that can also be used to represent the photocatalytic oxidation of such contaminants in both irradiated slurries and immobilized TiO_2 thin films.

2. Materials and methods

2.1. Photoreactors

Two batch cylindrical concentric photoreactors made of borosilicate glass were used (PR-A and PR-B, Fig. S1 in *Supporting Information (SI)*). Both reactors were characterized by an

annular reaction space and irradiated volume of 0.5 and 1.4 L, respectively. Each reactor was fitted with a sampling port, a magnetic stirrer, and water jacket for temperature control. The irradiation sources used were of two types: low-pressure mercury discharge UVA and UVC lamps with different dimensions and light outputs. The lamps were immersed axially inside quartz tubes located in the center axis of each reactor. The reactors and lamps specifications are summarized in Table 1. The reactors were operated with either a catalyst suspension of TiO_2 or with TiO_2-chitosan (CS/TiO_2) thin films immobilized on either small (76 mm × 26 mm × 2 mm) or large (210 mm × 65 mm × 2 mm) glass plates. In the immobilized catalyst configurations four small plates were fixed in the PR-A photoreactor near the external wall of the photoreactor, as shown in the Fig. S2(a). In contrast, one or two of the large plates were positioned in the PR-B photoreactor near to the lamp as shown in Fig. S2(b).

2.2. TiO_2-chitosan thin films

Titanium dioxide (AEROXIDE® P25, Evonik) with an elementary particle size of 30 nm, BET surface area 56 m^2/g and 75% anatase and 25% rutile was used. The preparation of the TiO_2–chitosan coated glass plates was performed following the procedure reported elsewhere [24]. Briefly, chitosan flakes (high molecular weight, Sigma-Aldrich) were dissolved in a pre-mixed solution of CH_3COOH and NaCl and stirred continuously for 12 h. The TiO_2 powder (10 g) was then added into the viscous solution, stirred continuously for 24 h and sonicated in an ultrasonic bath for 30 min (35 kHz, SONOREX RK 510H, Bandelin) to obtain a fine paste dispersion. Drops (1.5 cm diameter) of this paste dispersion were dispensed along the longitudinal centre of the glass plates (see Section 2.1) at 2 cm intervals and were dispersed over the glass surface by rolling with a glass cylinder. The coated glass plates were then dried in an oven at 105 °C for 1 hour. The entire coating procedure was repeated up to 4 layers. The coated plates were stored under darkness before use. The average CS/TiO_2 catalyst loading on

the small plates were 55 ± 2 mg (small plates) and 164 ± 3 mg (large plates). A detailed characterization of CS/TiO_2 thin films is reported elsewhere [23]. The mass content of TiO_2 in the films was > 93% according to thermogravimetric analysis.

2.3. Photocatalytic runs and analyses

Aqueous solutions were prepared with high purity water produced by a Millipore Milli Q water purification system (resistivity 18 MΩ cm^{-1}, total organic carbon < 1 ppb). Oxalic acid dihydrate and formic acid (Fluka, HPLC grade) were the model contaminants. In a typical experiment with suspended photocatalyst, a specified amount of TiO_2 was added to an aqueous solution of model contaminants contained in the photoreactor, under continuous turbulent stirring (rotational Reynolds number of 3485, see SI) to minimize mass transfer to the catalytic surface, and under darkness. These conditions were maintained for 30 min to equilibrate the species adsorption-desorption process, before irradiation was started. The experiments performed with the CS/TiO_2 thin films, were performed using the same procedure as above by immersing the coated plates into the contaminant aqueous solution. Samples collected at regular interval in preliminary experiments established that at such equilibration time, the concentration of FA and OA in solution reached a plateau. The reaction systems were operated at ambient temperature (22 ± 2 °C) at a pH 4.10 ± 0.15 during the entire irradiation time (120 min).

During the experiments, samples, collected at appropriate time intervals, were filtered through 0.20 μm PET filters (CHROMAFIL® PET-20/25) to remove the catalysts particles and promptly analyzed in a High-Performance Liquid Chromatograph (HPLC, Shimadzu), using a SUPELCOGEL H Carbohydrate column (250 mm x 4.6 mm) and UV detection at 210 nm to determine the concentration of FA and OA. The mobile phase flowing at 0.15 mL min^{-1} was 0.5% phosphoric acid in water. The rate of mineralization of the water contaminants and the

possible leaching of chitosan from the coated glass plates were evaluated by measuring the Total Organic Carbon (TOC) using a Shimadzu TOC-VCPN 5000 A. However, separate experiments (under darkness and under irradiation) performed with the CS/TiO_2 coated glass plates in ultra-pure water (pH ≈ 3 adjusted with diluted HCl) established that the leaching of chitosan from the glass support was insignificant. Although other studies have shown significant chitosan leaching from CS/TiO_2 immobilized on textile support [23], the higher temperature of 105°C used for the preparation of CS/TiO_2 films on glass (as compared with the 75°C used for the textile support) might strengthen the binding of chitosan on glass preventing its leaching.

Photon fluxes at 254 nm and 365 nm were determined with a radiometer (UVP- UVX) and by KI/KIO_3 chemical actinometry [25] using a a 0.6 M KI and 0.1 M KIO_3 in a 0.01 M $Na_2B_4O_7$ buffer solution. The photoproduct I_3^- in the overall photochemical reaction,

$$8\ I^- + IO_3^- + 3\ H_2O + h\nu \rightarrow 3\ I_3^- + 6\ OH^- \quad (1)$$

exhibited a strong absorption in the UV and was accurately quantified at λ = 355 nm (molar absorption coefficient ε = 26303 M^{-1} cm^{-1} in a 0.6 M KI/0.1 M KIO_3 solution), to avoid the interference from the other actinometer components. The quantum yield φ of this actinometer, at 254 nm, is 0.60. The irradiance from the low-pressure mercury lamps was calculated from [25]:

$$I_{act}(\mathrm{mWcm^{-2}}) = 29.17\frac{\left(A_{355,\ sample} - A_{355,\ blank}\right)\mathrm{V_{sample}(cm^3)}}{area(\mathrm{cm^2})\ \mathrm{t(s)}} \quad (2)$$

where t is the irradiation time, V is the liquid in the reactor volume and A is the absorbance measured at 355 nm. Sampling performed at different positions in the reaction space confirmed the reaction space as isoactinic.

The photon fluxes emerging from the UV lamps in the center of cylindrical reactors were also measured radiometrically and averaged along the axial and radial direction of the lamp wall, but using a correction factor [11, 26] to account for the sensor spectral response.

The morphology and elemental composition of the immobilized TiO_2-chitosan film was determined by SEM-EDS analysis (FE-SEM//Mira LMU, Tescan; Quantax, Bruker AXS Microanalysis) with an imaging resolution of 1-3 nm and High Brightness Schottky Emitter used as electron gun. When necessary, prior to SEM analysis, the sample was gold-coated by Au/Pt sputtering.

2.4. Reactor fluid-dynamics simulations

The cylindrical reactors PR-A and PR-B were operated in batch mode and under turbulent flow conditions. The flow Reynolds number for magnetic stirring was calculated from literature [11,34] (see also SI). Visimix Turbulent SV 2K7 was used to simulate the fluid dynamics and degree of mixing of the suspended solids in the photoreactors. In these simulations the fluid was a Newtonian fluid and the density, and the dynamic viscosity were those of water at 20°C. The simulations of the velocity flow field inside the reactor were performed considering the geometry of the reactor, the calculated Reynolds numbers and the tangential flow of the magnetic stirrer. The TiO_2 particles diameter and the density of the solid phase were as reported in the manufacturer's material safety data sheets.

3. Modeling approach

3.1. Radiation emission and absorption-scattering model

The radiation field inside the aqueous suspension of catalysts was modeled by the SFM [11, 27-29]. In this model, four sub-models are combined with the material balance: the radiation emission model, the radiation absorption-scattering model, the fluid-dynamics model and the kinetic model.

The radiation sources are considered as long slim tubes which can be mathematically presented as an ideal linear radiation source: perfect cylinders in which the ratio of the radius to the length is rather small. Therefore, the cylindrical lamp was modeled as a line source with each point emitting radiation in every direction and isotropically (Linear Source Spherical Emission, LSSE model) [30]. Furthermore, it was assumed that the radiation emitted by each point of the line source was equal along the axial direction of the lamp.

The incident photon flux at the inner wall of the reactor can then be written using dimensionless parameters [27]:

$$I_0 = I_{(\eta R),z^*} = \frac{S_L}{4\pi\eta R}\left\{\arctan\left[\frac{\beta}{2}\left(2\alpha z^* - \alpha + 1\right)\right] - \arctan\left[\frac{\beta}{2}\left(2\alpha z^* - \alpha - 1\right)\right]\right\} \quad (3)$$

where S_L is the radiation emission of the lamp per unit time and unit length of the lamp ($S_L = 2\pi R_L I_w$), I_w is the radiation intensity measured at the lamp wall for the applied irradiation (UVA or UVC), α and β are geometrical design parameters of an annular photoreactor (α = H/L and β = L/ηR, respectively) and z^* is the dimensionless axial coordinate, $z^* = z/H$. H is the reactor length, L is the length of the cylindrical lamp in which radiation can be considered to be uniformly emitted, and ηR is the outer radius of the quartz tube housing the cylindrical lamp (Fig. S1 in SI). Note that for the UVA polychromatic irradiation source, I_w was calculated by averaging the emission spectrum of the lamp weighted with the absorption

spectrum of the photocatalyst, as shown elsewhere [11, 26]. Moreover, the refraction of light by the quartz tube housing the lamp was neglected.

For an infinitely long annular photocatalytic reactor, the local volumetric rate of photon absorption (LVRPA) at a point (r, z) in the reaction space calculated with the SFM in cylindrical coordinate is [11,27];

$$e^{a}_{r,z} = \frac{\tau_{app} I_0}{\omega_{corr}(1-\gamma)} \frac{\eta}{(1-\eta)\mathrm{R}} \left[\left(\omega_{corr} - 1 + \sqrt{1-\omega^2_{corr}} \right) \exp(-\tau_{app} r^*) + \gamma \left(\omega_{corr} - 1 - \sqrt{1-\omega^2_{corr}} \right) \exp(-\tau_{app} r^*) \right] \quad (4)$$

where τ_{app} is the apparent optical thickness, ω_{corr} is the corrected scattering albedo, η is the ratio of internal to external radius of the annulus, γ is a SFM dimensionless parameter and r^* is the dimensionless reaction space radial coordinate (Table S1, SI). The optical properties of the photocatalyst, σ^* and κ^*, are the specific scattering and absorption coefficients per unit mass of catalyst, respectively. The specific adsorption and scattering coefficients of TiO_2 P25 at 365 nm and 254 nm were taken as $\sigma^*_{UVA} = 1163$ m^2 kg^{-1}, $\kappa^*_{UVA} = 187$ m^2 kg^{-1} and $\sigma^*_{UVC} = 625$ m^2 kg^{-1}, $\kappa^*_{UVC} = 1192$ m^2 kg^{-1} [11,31]. Isotropic photon scattering was reasonably assumed, thus the probabilities of forward, backward and side scattering respectively, used in the SFM were equal to $p_f = p_b = p_s = 1/6$.

Since the PR-A and PR-B reactors were well-mixed systems, the concentration of reacting species inside the reactor were considered to be spatially uniform, although the local rate of reaction was spatially dependent, since the LVRPA in slurries varies within the reactor volume and the incident photon flux in immobilized films varies with position. However, since the high turbulence generated by the mixing device provides sufficient transversal mixing in the reactor, continuously exposing new catalyst to areas of high irradiance, the LVRPA in slurries evaluated from Eq. (4) can be averaged across the reactor volume and treated as a lumped parameter (e^{a}_{Lump}, Eq. 5) in the kinetics rate laws of FA and OA oxidation.

$$e^{a}Lump = \frac{1}{V_R} \int_{V_R} \left(e^{a}{}_{r,z} \right) dV_R \tag{5}$$

The rate of photon absorption in systems using immobilized photocatalyst depends on the incident photon flux on the photocatalyst surface [32,33] which can be estimated from the LSSE model:

$$I_{0,\mathrm{f}}(r,z) = \frac{I_w R_\mathrm{L}}{2R_i} \left\{ \arctan\left[\left(\frac{z-x}{R_i} \right) \right] - \arctan\left[\left(\frac{z-x-L}{R_i} \right) \right] \right\} \tag{6}$$

where I_w is the radiation intensity measured at the lamp wall, R_L and L are lamp radius and length, respectively, x is a geometrical design parameter of an annular photoreactor which for a perfectly centered lamp is [x = (H - L) / 2] (Fig. 2) and z is the axial coordinate. Since the TiO_2-chitosan films was immobilized on flat plates, the position at the photocatalyst surface was located by the cartesian coordinates (x, y, z). The incident photon flux over the entire catalytic surface of the plates was determined after transforming the coordinates from cartesian to cylindrical (r, z) (Eq. (6), Figs. 1a and b), where R_i matches the radial distance of each point on the photocatalysts surface in the annular reaction space. This calculation was straightforward for PR-B, since the plates were parallel to the lamp. Moreover, the most distant point on the film surface ($R_{\mathrm{x,f}}$) matched the reactor radius minus the thickness of the glass plate (δ_{gp}), thus the nearest point ($R_{0,\mathrm{f}}$) was calculated using simple geometry (Fig. 2). In contrast the glass plates in PR-A were inclined over the vertical, thus the radial distance of the photocatalysts surface varied along the z axis. At the bottom of the glass plate (z_0), the nearest point ($R_{0,\mathrm{f}}(z_0)$) was determined from the difference between the reactor radius and the known distance of the center of the plate from the reactor wall. Simple geometry was then applied to find the furthermost point ($R_{\mathrm{x,f}}(z_0)$):

$$R_{x,f}(z_0) = \sqrt{\left(R_{0,f}(z_0) \right)^2 + \left(d_{gp} / 2 \right)^2} \tag{7}$$

where d_{gp} is the plate width. Similarly, the radial coordinate of the farthest point at the uppermost part of the plate ($R_{x,f}(z_x)$) equaled the reactor radius minus the plate thickness and was used to determine the nearest point at z_x:

$$R_{0,f}\left(z_x\right)=\sqrt{\left(R_{x,f}\left(z_x\right)\right)^2-\left(d_{gp}/2\right)^2} \tag{8}$$

In Eq. 8, z intervals were actually projections of the glass plate height (h_{gp}) (Fig 1b). For each z interval, radial the coordinates were determined from $R_{0,f}(z_i)$ to $R_{x,f}(z_i)$.

$$R_{0,f}\left(z_i\right)=R_{0,f}\left(z_{i-1}\right)+\Delta R_0 \tag{9}$$

$$R_{x,f}\left(z_i\right)=\sqrt{\left(R_{0,f}\left(z_i\right)\right)^2+\left(d_{gp}/2\right)^2} \tag{10}$$

and

$$\Delta R_0=\frac{R_{0,f}\left(z_x\right)-R_{0,f}\left(z_0\right)}{N} \tag{11}$$

where N is the selected number of intervals used for the calculation.

The incident photon flux was determined for each (r, z) point on the photocatalysts surface, and the average value was calculated from Eq. 12 for the same reason as explained previously.

$$I_{0,\,\mathrm{Lump}}=\frac{\sum_i\left(\int_{z_i}^{R_{x,z_i}}\int_{R_{0,z_i}} I_{0,f}\left(r,z\right)drdz\right)}{S} \tag{12}$$

where S is the illuminated photocatalyst surface area.

3.2. Formic and oxalic acid reaction kinetic models and mass balance

The complex pathway of adsorption and photodecomposition of oxalic acid onto TiO_2 postulated by [35], was used as the basic mechanistic scheme to formulate the reaction kinetics rate law of photocatalytic oxidation over irradiated TiO_2 slurry suspension [11,21]. According to this mechanism, the adsorption of oxalate on aqueous suspensions of TiO_2

proceeds through the formation of two kinds of surface complexes: a more stable bidentate structure (named species A hereafter) and a more labile one (named species B hereafter), with the sigma carbon–carbon bond either parallel or perpendicular to the TiO_2 surface, respectively (Fig. S3). Upon irradiation of the catalyst suspension, sterically exposed species B are readily attacked, via a faster $OH^{\bullet}$ mechanism**,** while direct hole transfer oxidation is responsible for the decomposition of species A. In consequence, during irradiation of the suspension the surface coverage of species A and B on TiO_2 dynamically changes, with a progressive displacement of species B by species A, since species B is depleted at a faster rate than A. Therefore, the photocatalytic degradation of OA is characterized by two parallel, simultaneous reaction pathways shown in Table S2. Under the steady-state approximation for hydroxyl radicals, unstable reaction intermediates, holes and electrons, the simplified expression for the local OA reaction rate is [11, 21]:

$$-r_{\mathrm{OA}}(\underline{x},t)=\left\{k_{OA,B}\theta(t)\left[\mathrm{OA}\right]_{aq}+k_{OA,A}\left[1-\theta(t)\right]\sqrt{\left[\mathrm{OA}\right]_{aq}}\right\}\sqrt{e^{a}(\underline{x})} \tag{13}$$

where the fraction of B sites is characterized by a decreasing linear function proportionally to LVRPA (Eq. 14) while $\underline{x}$ is the space vector that determines the position in the (z, r, φ) coordinate system.

$$\theta(\mathrm{t}) = \beta' [\mathrm{OA}]_{\mathrm{t}=0}[1-\alpha' \mathrm{t}\, e^{a}] \tag{14}$$

Considering that the LVRPA can be lumped (Eq. 5 or 12), Eq. (13) becames:

$$-r_{\mathrm{OA}}(t)=\left\{k_{OA,B}\theta(t)\left[\mathrm{OA}\right]_{aq}+k_{OA,A}\left[1-\theta(t)\right]\sqrt{\left[\mathrm{OA}\right]_{aq}}\right\}\sqrt{e^{a}{}_{Lump}} \tag{15}$$

This reaction kinetics rate law for the overall photocatalytic degradation of oxalic acid combines two mechanisms working in parallel which is embossed by the combination of an apparent first order kinetics for the $^{\bullet}OH$ radical on AO and a square root dependence to the concentration of AO representing the hole-trapping oxidation pathway. Moreover, the square root dependence to the LVRPA in Eq. (15) represents the region typical for well-irradiated

reacting systems, while for lower photon fluxes a linear dependence should be considered. The intrinsic reaction rate constants $k_{OA,A}$ and $k_{OA,B}$ and the parameters α', β', were determined in our previous study [11].

Regarding the oxidation of formic acid, OH radical attack of FA by the Fenton reaction in aqueous media proceeds through the formation of radical species, which recombine to OA [36]. However, OA was not observed during the decomposition of FA over irradiated TiO_2 suspensions. Unlike AO, the adsorption of FA on TiO_2 yields one complex, whereby the C-H bond is perpendicular to the TiO_2 surface, ressembling the OA labile specie B. This observation matches the reaction mechanism of attack on the FA α-C-H bond by •OH radical followed by hydrogen abstraction from the molecule [37]. Thus according to this mechanism formic acid decomposes in a single step, yielding carbon dioxide and water. On this basis, the FA adsorption and photodegradation on TiO_2 was modeled by the Langmuir-Hinshelwood kinetic model [38,39], and by Eq. (16):

$$-r_{FA} = \frac{k_{FA} K_{L,FA} [FA]}{1 + K_{L,FA} [FA]} \sqrt{e^{a}_{Lump}} \tag{16}$$

where k_{FA} and $K_{L,FA}$ are the apparent reaction rate constant and the binding constant.

The photocatalytic reaction of AO and FA on immobilized photocatalyst was therefore modeled by the same reaction kinetics models, with the radiation absorption term expressed as the product of the thin film absorption coefficient (μ, m^{-1}) and the incident photon flux at photocatalyst surface ($\mu I_{0,\,Lump}$) , Eqs. (17-18) respectively.

$$-r_{OA}(t) = \left\{ k_{OA,B}\theta(t)[OA]_{aq} + k_{OA,A}[1-\theta(t)]\sqrt{[OA]_{aq}} \right\} \sqrt{\mu I_{0,Lump}} \tag{17}$$

$$-r_{FA} = \frac{k_{FA} K_{L,FA} [FA]}{1 + K_{L,FA} [FA]} \sqrt{\mu I_{0,Lump}} \tag{18}$$

The mass balance for OA and FA species in a well-mixed, constant volume and constant temperature batch reactor was:

$$-r_i = \frac{d[X_i]}{dt} \tag{19}$$

where X_i refers to the concentration of either AO or FA in water. Since the reactors were operated under high turbulence, the initial condition to solve the reacting flow over the photocatalytic films was $X_{i,surface} = X_{i,bulk}$.

The OA and FA kinetic parameters were determined by minimizing an objective function of the sum of the square of the errors between the species concentrations calculated by the model and those determined experimentally.

4. Results and discussion

4.1. Photon radiation absorption and incident photon flux

The radiation field in both suspended or immobilized TiO_2 photoreactors was determined to evaluate the distribution of the LVRPA or LSRPA and therefore the lumped values of the these to be replaced in the contaminants rate laws (Eq. 15-18).

The transversal profile of the e^a (Eq. (4)) in the cylindrical photoreactors using the suspended photocatalyst is expected to vary with reactor geometry and photocatalyst dosage. As shown in Fig. 3, a sharp gradient of the dimensionless LVRPA was observed for the reaction conditions analyzed, meaning that the majority of the incident radiation was absorbed in the region in proximity to the light source, while a significant portion of the reactor away from the light source was poorly illuminated. However, since the cylindrical reactor was magnetically stirred at a high rate, it may also be inferred that the reactor behaved as a pseudo-isoactinic reactor. In consequence, it was possible to calculate from the discrete values of the LVRPA, the volume averaged e^a_{Lump} (Eq. 5) which can then be directly used to model the impact of radiation adsorption in the contaminant rate law. The pseudo-homogeneity of mixing in the reactor was demonstrated by an analysis of the hydrodynamics conditions in the reactor, which also included the radial and axial distribution of the solid particles in the PR-A

and PR-B reactors. Figure S4 (SI) shows the turbulent flow patterns in the two reactors and the corresponding tangential velocities generated. The corresponding calculated Reynolds numbers generated by the rotation of the stirrer bar and simulated degrees of suspension are reported in Table S3 (SI) along with the other relevant hydrodynamic properties and properties of the slurry suspension in the PR-A reactor. The spatial distribution of the solid particles in the PR-A reactor for an axial cross- section of the reactor is shown in Fig. S5. The chaotic flow patterns in the reactor allows the consideration that such reactors behaved as pseudo-isoactinic. In such pseudo-isoactinic system, the hypothetical photocatalytic particle (P1) close to the irradiation source ($\xi^* \rightarrow 0$) absorbing a high rate of photons, can move towards the outer reactor wall in a matter of milliseconds due to the strong developed tangential flow. In consequence, the photocatalytic reaction initiated at ($\xi^* \rightarrow 0$) is expected to continue at $\xi^* \rightarrow 1$. Vice versa, another photocatalytic particle (P2) that was originally at the outer wall would be brought instantly to the inner wall ($\xi^* \rightarrow 0$). The calculated circulation rate constant of P1 and P2 between the inner and the outer reactor wall is of the order of milliseconds and this has the same order of magnitude as the photocatalytic surface reaction phenomena [40]. Thus, the LVRPA was averaged across the reactor volume and treated as lumped parameter (e^a_{Lump}, Eq. 5) in the kinetics rate laws of FA and OA oxidation. The value of e^a_{Lump} calculated from Eq. 5 in the PR-A and PR-B are reported in Table 2 for a range of different experimental conditions. The e^a_{Lump} values calculated for 0.4 g L^{-1} of catalyst irradiated with UVC light correspond to the local e^a values calculated at (ξ^*= 0.1346, z^* = 0.5) and (ξ^*= 0.1299, z^* = 0.5) points in the reaction space, for PR-A and PR-B, respectively. This radial distance in the annular space matches the reactor radius of 1.21 and 1.63 cm, respectively. Relatively high values of e^a_{Lump} suggest a well-irradiated reactor, with more appropriate radius-to-length ratio in PR-B.

The incident radiation field over the TiO_2-chitosan films immobilized on the flat glass plates immersed in PR-A and PR-B radiation was determined by transforming the cartesian coordinates of the glass plates to a cylindrical coordinate system. This allows a two-dimensional analysis of the incident photon flux on the photocatalytic film surface along the (r, z) plane, as shown in the results in Fig. 4. The distribution was longitudinally asymmetrical over the inclined plates (PR-A), thus yielding higher incident photon fluxes in the lower half of the plates, i.e. the region nearer to the lamp (Fig. 2b), while it was symmetrical over the vertically mounted plates (PR-B). Moreover, the incident radiation and irradiated area was less intense in the plates irradiated with UVA in comparison to those irradiated with UVC since the emission radiant flux was higher in the latter. The gradual decrease of the incident photon flux along the plate width (Fig. 4) results from the increase of the radial distance from the light source. Likewise, the considerations made for the slurry reactors, the intense mixing in the reactors allows the assumption that the reactants are uniformly distributed over the photocatalytic plates, thus the average value of the incident photon flux on the plates (Table 2) was used in the rate laws describing the contaminants degradation (Eq. 17-18). Those values correspond to the incident photon flux calculated at the (r, z) positions of the plates connected with green lines (Fig. 4).

4.2. Photocatalytic oxidation of formic and oxalic acid in slurry reactors

Photocatalytic degradation experiments of single-component FA or OA and with a mixture of them in aqueous solution were performed in PR-A and PR-B with different light sources (UVA or UVC) to validate the model developed and supporting assumptions over a diverse range of experimental conditions. FA and OA were chosen as model water contaminants since the photolytic degradation of these pollutants under both UVC and UVA irradiation was found insignificant in both reactors and also since their photocatalytic degradation follows a

well-known mechanism described by defined kinetic models (Eqs. 13-18). Detailed kinetics investigations of degradation of FA and OA including the formation of oxidation products have been presented in other studies and were beyond the purpose of this study [21,35]. Due to the high hydrodynamic turbulence in the reactors and respective small molecular size and the affinity toward positively charged photocatalysts surface, the rate of mass transfer of FA and OA on the film was considered to be much faster than their photocatalytic reaction, thus the rate of disappearance of the contaminants was controlled by the chemical reaction over the photocatalytic film (reaction kinetics regime). Moreover, since the TiO_2-chitosan photocatalytic film was non-porous, the adsorption and reaction occurred in the upper layer of the thin film exposed to light [41]. For the same reason, OH radicals did not compete with chitosan since these could not diffuse into the core of the immobilized particles [41].

The kinetics of degradation of FA and OA with slurry suspensions of TiO_2 are shown in Fig. 5. The results of photocatalytic oxidation of the carboxylic acids confirmed that "small" negatively charged molecules were easily adsorbed on the TiO_2 surface under the acidic conditions used, followed by the oxidation according to the corresponding reaction pathways on the surface. Both studied acids dissociate to corresponding anions, i.e. formate and oxalate that can be easily adsorbed on the TiO_2 surface, which is positively charged at pH 4.10 ± 0.15 (point of zero charge of TiO_2 pH 6.3). The developed models for OA and FA photocatalytic oxidation in the reactors operated with a slurry TiO_2 suspension fitted well the experimental results obtained with solutions of single component of OA or FA (Fig. 5a-b) and in addition using a mixture of them (Fig. 5c-e), at different initial concentrations and using different reactors configurations and light sources. The intrinsic kinetic parameters determined from the matching of the model to the experimental results are shown in Table 3. The single-step oxidation process that was assumed for the short-chain carboxylic acids [38] was confirmed

by the match between the theoretical TOC of OA and FA calculated from the model and the experimentally measured TOC during the entire time span.

4.3. Photocatalytic oxidation of formic and oxalic acid in immobilized films

Fig. 6 shows the morphology of the TiO_2-chitosan thin films made of spherical aggregates containing macropores. SEM magnification revealed a core-shell chitosan-TiO_2 structure made of a thick TiO_2 shell (7.10 μm in Fig. 6b) enveloping a chitosan core. EDS mapping analysis of Ti and C revealed the prevalent existence of Ti in the top layer from the TiO_2 phase, while C emerged from the bottom layer from the chitosan phase.

It can be inferred that both slurries suspensions and immobilized TiO_2 might exhibit the same spectral absorption edges. UVA photons are exclusively absorbed by TiO_2 ($\lambda < 384$ nm), while UVC photons could be absorbed by both TiO_2 and chitosan ($\lambda < 290$ nm), however, since the penetration depth of UVC photons on TiO_2 films is less than 500 nm [31], it can be reasonably assumed that the incident photons on the immobilized thin films were absorbed within the TiO_2 shell only.

The results of the photocatalytic decomposition of FA an OA over immobilized TiO_2-chitosan thin films are shown in Fig. 7. Generally, lower apparent reaction rates and lower mineralization yields were observed in comparison with the process with suspended photocatalyst since the overall surface area of TiO_2 exposed to light irradiation was smaller. The intrinsic reaction kinetic coefficients of FA and OA degradation determined by modeling the experimental results obtained with the slurry TiO_2 suspension (k_{FA}, $k_{OA,A}$, $k_{OA,B}$, Table 3) were further used in the contaminant rate laws, to model the experimental results obtained with the immobilized TiO_2-chitosan thin films. Experiments were performed with PR1 and PR2 reactors configurations, under UVA or UVC irradiation and under diverse experimental conditions (Fig. 7).

By fitting the model for the photocatalytic thin-film to the experimental results (Fig. 7), the unknown apparent absorption coefficient of TiO_2 (μ_{app}) of the TiO_2-chitosan thin films was determined (Table 3). This value of (μ_{app}) also equals the product of the "apparent" specific absorption coefficient of TiO_2 in the film (κ_{app}) and the concentration of TiO_2 in the reaction space determined as the total mass of TiO_2 immobilized over the glass plates divided the reactors volumes ($\mu_{app} = \kappa^*_{app,film}\, c_{cat}$). Thus, the calculated $\kappa^*_{app,film}$ (50.5 ± 5.6 $m^2\ kg^{-1}$ with UVA irradiation and 321.8 ± 35.8 $m^2\ kg^{-1}$ with UVC irradiation (Table 3)) were compared with the specific absorption coefficients (κ^*) of TiO_2 P25 (187 $m^2\ kg^{-1}$ under UVA [11] and 1192 $m^2\ kg^{-1}$ under UVC [42]). From this comparison, it became clear that in all reactor configurations the ratio between apparent and calculated absorption coefficients (Eq. 20) remained practical constant and equaled ε = 0.27 ± 0.03 independently of the light source, reactor configuration or number of photocatalytic plates.

$$\varepsilon = \frac{\kappa^*_{app,film}}{\kappa^*} \tag{20}$$

Thus, it was determined that only a fraction of the immobilized thin film (27%) was photocatalytically active. This may be attributed to the thickness and morphology of the TiO_2-chitosan thin films as-prepared (Fig. 6) which presents macropores and only let a fraction of the film mass to be irradiated (by direct irradiation and by multiple photon scattering) and be exposed to the species mass transfer.

The methodological approach presented in this study can be extended to further design of photocatalytic systems utilizing photocatalytic thin films. Thus, after determining the "specific" absorption coefficient of the thin film immobilized over a specific support by fitting the model to laboratory experimental results, then the absorption coefficient of the thin film in other reactor configurations can be calculated by considering the mass of catalyst immobilized on the supports.

The simultaneous use of two large photocatalytic plates in PR-B (Fig. 7d) resulted in approximately double OA and FA oxidation rates and related mineralization extents compared to results with a single plate (Fig. 7c), thus doubling the exposed surface area (or mass of catalyst) doubled the contaminants removal rates. Moreover, the results obtained with UVC irradiation were comparable to those obtained with a slurry catalyst suspension (Fig. 5e). Despite the smaller amount of catalyst used in the immobilized systems in comparison to the slurry, the rate of photon absorption ($\mu_{app} I_{o,lump}$) was significantly larger than the lumped VRPA in the slurry (e^{a}_{Lump}) and this compensated for the smaller amount of catalyst surface area effectively irradiated. This aspect was more evidenced under UVC irradiation since the specific absorption coefficient of TiO_2-P25 in the UVC was significantly higher than in the UVA, thus the volumetric region of the reactor effectively irradiated with photons was significantly smaller. On the contrary, in immobilized systems, the surface area of catalyst irradiated remain unaffected by the wavelength of irradiation, thus since $\kappa^*_{UVC} >> \kappa^*_{UVA}$, higher rate of contaminant degradation under UVC were obtained and these were comparable to those obtained in slurry systems under the operating conditions employed. This result was achieved also since the rate of species mass transfer from the bulk to the catalytic surface was maximized due to intense turbulence in the reactors, hence the catalytic surface was promptly replenished with fresh reactant. Mass transfer limitations take full control of the contaminants removal rates in photocatalytic reactors utilizing immobilized photocatalysts operated under low turbulence levels or under laminar flow conditions (i.e., $X_{i,surface} << X_{i,bulk}$). Thus, under poor mixing conditions, these reactor systems are usually outperformed by slurry photocatalytic systems. It is therefore important to maximize the surface area of the immobilized photocatalyst exposed to both photons and reacting species while simultaneously maintaining high fluid turbulence levels, such as in flow through or in cross flow membrane photocatalytic reactors or even by using a static mixer as a photocatalyst support [43].

Many other factors can influence the intrinsic reaction kinetics of photocatalytic processes such as catalyst structure, band-gap, morphology, surface area and catalyst agglomeration. Here we have shown a simple modeling approach that can be applied to predict the photocatalytic oxidation of target water contaminants in both slurry suspensions and immobilized photocatalyst and different photoreactor geometries/conditions, providing that the same reaction mechanism holds. The important aspect for such approach is the evaluation of the photocatalyst optical properties (σ_λ* and κ_λ*) in the reaction fluid and under the prevalent mixing conditions, which are a function of irradiation wavelength λ. Thus, if the catalyst structure and/or band-gap are changed then first step of the modeling procedure is to re-evaluate the optical properties of the photocatalyst. Here we have simplified this aspect by calculating spectral-averaged optical properties (σ* and κ*), to reduce the complexity of the model. All other effects (e.g., temperature, catalyst morphology, porosity, surface charge) are incorporated in the intrinsic kinetic constants. Of course, if the same photocatalyst is used to treat a different target contaminant, then the rate laws may need to be reformulated to account for the adsorption/reaction mechanism and the kinetic constants need to be re-evaluated. However, in this study we have shown that if we only change the reactor configuration from slurry to immobilized films, then the same kinetics parameters can model the experimental results. The impact of water matrix is also very important since dissolved species and suspended solids can affect the reaction kinetics and the optical properties of catalyst. To account for these effects, the reaction mechanism of photocatalytic degradation of water contaminants would need to include the impact of the various species (e.g., anions/cations, natural organic matter) thus the water contaminants rate laws would need to be revisited.

5. Conclusions

This study has demonstrated a modeling methodology for the photocatalytic oxidation of a mixture of water contaminants using either suspended or immobilized photocatalyst. It has shown that the kinetic parameters of photocatalytic oxidation OA and FO determined in a slurry suspension of TiO_2 under diverse experimental conditions can also be used to model their decomposition over TiO_2-chitosan thin film immobilized on flat glass plates. The intrinsic nature of the kinetic parameters was demonstrated over reactors of different geometries, with the use of different light sources (UVA or UVC) and using single component and mixtures of OA and FO. Moreover, it was shown that lumping the LVRPA or the LSRPA can simplify the modeling procedure, providing that intense turbulent mixing is maintained in the reactors.

The method shown allowed the estimation of the apparent absorption coefficient of immobilized photocatalytic thin films and of the effective fraction of the immobilized thin film that is photocatalytically active. This modeling approach would therefore be useful to guide the optimization of thin film composition and thickness and its spatial distribution in a photocatalytic reactor. The use of immobilized photocatalysts may overcome the need of a catalyst recovery stage involving microfiltration in slurry systems, which may add to the capital and operating costs of the water treatment process, however, for such reactors it is key that high turbulence levels are maintained near the photocatalytic walls to eliminate mass transfer limitations. Overall, this study has shown how the performance of either slurry or immobilized photocatalyst photocatalytic system can be predicted from intrinsic kinetic parameters and how this can guide photoreactors design.

Acknowledgements

This work was supported by European Regional Development Fund (ERDF) under the project "Waste & Sun for photocatalytic degradation of micropollutants in water" (OS-Mi), KK.01.1.1.04.0006.

References

[1] I. Grčić, D. Vujević, K. Žižek, N. Koprivanac, Treatment of organic pollutants in water using TiO_2 powders: Photocatalysis vs. Sonocatalysis, React. Kinet. Mech. Catal. 109 (2013) 335-354.

[2] D. Shahidi, R. Roy, A. Azzouz, Advances in catalytic oxidation of organic pollutants-Prospects for thorough mineralization by natural clay catalysts, Appl. Catal. B: Environ. 174–175 (2015) 277-292.

[3] I. Grčić, D. Vujević, J. Šepčić, N. Koprivanac, Minimization of organic content in simulated industrial wastewater by Fenton type processes: A case study, J. Hazard. Mater. 170 (2009) 954-961.

[4] V.K. Saharan, D.V. Pinjari, P.R. Gogate, A.B. Pandit, Advanced Oxidation Technologies for Wastewater Treatment: An Overview, in: Industrial Wastewater Treatment, Recycling and Reuse (Eds. V. V. Ranade, V. M. Bhandari), Butterworth-Heinemann, UK, 2014, pp. 141-191.

[5] M. Antonopoulou, E. Evgenidou, D. Lambropoulou, I. Konstantinou, A review on advanced oxidation processes for the removal of taste and odor compounds from aqueous media, Water Res. 53 (2014) 215-234.

[6] M. Nan Chong, A.K. Sharma, S. Burn, C.P. Saint, Feasibility study on the application of advanced oxidation technologies for decentralised wastewater treatment, J. Clean. Prod. 35 (2012) 230-238.

[7] J.R. Alvarez-Corena, J.A. Bergendahl, F.L. Hart, Advanced oxidation of five contaminants in water by UV/TiO_2: Reaction kinetics and byproducts identification, J. Environ. Manage. 181 (2016) 544-551

[8] H. Choi, S.R. Al-Abed, D.D. Dionysiou, E. Stathatos, P. Lianos, Chapter 8: TiO_2-Based Advanced Oxidation Nanotechnologies for Water Purification and Reuse, in: Sustainable Water for the Future: Water Recycling versus Desalination (Eds. I. C. Escobar, A. I. Schäfer), Elsevier, 2010, pp. 229–254.

[9] J.F. Montoya, J.A. Velasquez, P. Salvador, The direct–indirect kinetic model in photocatalysis: A reanalysis of phenol and formic acid degradation rate dependence on photon flow and concentration in TiO_2 aqueous dispersions, Appl. Catal. B: Environ. (2009) 50–58.

[10] P.Z. Araujo, P. J. Morando, E. Martínez, M.A. Blesa, Time evolution of surface speciation during heterogeneous photocatalysis: Gallic acid on titanium dioxide, Appl. Catal. B: Environ. 125 (2012) 215– 221.

[11] I. Grčić, G. Li Puma, Photocatalytic Degradation of Water Contaminants in Multiple Photoreactors and the Evaluation of Reaction Kinetics Constants Independent of Photon Absorption, Irradiance, Reactor Geometry and Hydrodynamics, Environ. Sci. Tech. 47 (2013) 13702-13711.

[12] E. R. Bandala, C. A. Arancibia-Bulnes, S. L. Orozco, C. A. Estrada, Solar photoreactors comparison based on oxalic acid photocatalytic degradation, Sol. Energy 77 (2004) 503-512.

[13] R.W. Matthews, Photocatalytic oxidation of organic contaminants in water: An aid to environmental preservation, Pure Appl. Chem. 64 (1992) 1285-1290.

[14] V. Loddo, L. Palmisano, T. Marino, R. Molinari, Chapter 23: Membranes for photocatalysis in water and wastewater treatment, in: Woodhead Publishing Series in

Energy, Advanced Membrane Science and Technology for Sustainable Energy and Environmental Applications (Eds. A. Basile, S. Pereira Nunes), Woodhead Publishing, 2011, pp. 746-768.

[15] M.F.J. Dijkstra, A. Michorius, H. Buwalde, H.J. Panneman, J.G.M. Winkelman, Comparison of the efficiency of immobilized and suspended systems in photocatalytic degradation, Catal. Today 66 (2001) 487-494.

[16] T.A. McMurray, J.A. Byrne, P.S.M. Dunlop, J.G.M. Winkelman, B.R. Eggins, E.T. McAdams, Intrinsic kinetics of photocatalytic oxidation of formic and oxalic acid on immobilised TiO_2 films, Appl. Catal. A: General 262 (2004) 105-110.

[17] J.A. Byrne, B.R. Eggins, N.M.D. Brown, B. McKinney, M. Rouse, Immobilisation of TiO_2 powder for the treatment of polluted water, Appl. Catal. B: Environ. 17 (1998) 25-36.

[18] A.K. Ray, A. Beenackers, Development of a new photocatalytic reactor for water purification, Catal. Today 40 (1998) 73-83.

[19] J. Kulas, I. Rousar, J. Krysa, J. Jirkovsky, Photocatalytic degradation rate of oxalic acid on the semiconductive layer of n-TiO_2 particles in the batch mode plate reactor Part I: Mass transfer limits, J. Appl. Electrochem. 28 (1998) 843-853.

[20] G. Li Puma, B. Toepfer, A. Gora, Photocatalytic oxidation of multicomponent systems of herbicides: Scale-up of laboratory kinetics rate data to plant scale, Catal. Today. 124 (2007) 124-132.

[21] R.L. Pozzo, R.J. Brandi, A.E. Cassano, M.A. Baltanás, Photocatalytic oxidation of oxalic acid in dilute aqueous solution, in a fully illuminated fluidized bed reactor, Chem. Eng. Sci. 65 (2010) 1345-1353.

[22] C.B. Mendive, T. Bredow, J. Schneider, M. Blesa, D. Bahnemann, Oxalic acid at the TiO_2/water interface under UV(A) illumination: Surface reaction mechanisms, J. Catal. 322 (2015) 60–72.

[23] I. Grčić, D. Vrsaljko, Z. Katančić, S. Papić, Purification of household greywater loaded with hair colorants by solar photocatalysis using TiO_2-coated textile fibers coupled flocculation with chitosan, J. Water Process. Eng. 5 (2015) 15-27.

[24] Z. Zainal, L. Kong Hui, M.Z. Hussein, A.H. Abdullah, I. Hamadneh, R. Moh'dKhair, Characterization of TiO_2–chitosan/glass photocatalyst for the removal of a monoazo dye via photodegradation–adsorption process, J. Hazard. Mater.164 (1) (2009) 138–145.

[25] R.O. Rahn, M.I. Stefan, J.R. Bolton, E. Goren, P.S. Shaw, K.R. Lykke, Quantum yield of the iodide-iodate chemical actinometer: Dependence on wavelength and concentration, Photochem. Photobiol. 78 (2003) 146-152.

[26] J. Colina-Marquez, F. Machuca-Martínez, G. Li Puma, Photocatalytic mineralization of commercial herbicides in a pilotscale solar CPC reactor: Photoreactor modeling and reaction kinetics constants independent of radiation field, Environ. Sci. Technol. 43 (2009) 8953−8960.

[27] G. Li Puma, A. Brucato, Dimensionless analysis of slurry photocatalytic reactors using two-flux and six-flux radiation absorption scattering models, Catal. Today 122 (2007) 78−90.

[28] G. Li Puma, J. N. Khor, A. Brucato, Modeling of an annular photocatalytic reactor for water purification: Oxidation of pesticides, Environ. Sci. Technol. 38 (2004) 3737−3745.

[29] B. Toepfer, A. Gora, G. Li Puma, Photocatalytic oxidation of multicomponent solutions of herbicides: Reaction kinetics analysis with explicit photon absorption effects, Appl. Catal. B: Environ. 68 (2006) 171−180.

[30] S.M. Jacob, J.S. Dranoff, Radial scale-up of perfectly mixed photochemical reactors, Chem. Eng. Prog. Symp. Ser. 62 (1966) 47−55.

[31] I. Grčić, G. Li Puma, Six-flux absorption-scattering models for photocatalysis under wide-spectrum irradiation sources in annual and flat reactors using catalysts with different optical properties, App. Catal. B 211 (2017) 222-234.

[32] I. Salvadó-Estivill, A. Brucato, Li Puma, G. Two-dimensional modeling of a flat-plate photocatalytic reactor for oxidation of indoor air pollutants, Ind. Eng. Chem. Res. 46 (2007) 7489-7496.

[33] B. Plavac, I. Grčić, I. Brnardić, V. Grozdanić, S. Papić, Kinetic study of salicylic acid photocatalytic degradation using sol–gel anatase thin film with enhanced long-term activity, React. Kinet. Mech. Catal. 120 (2017) 385-401.

[34] G. Halász, B. Gyüre, M. Jánosi, K. G. Szabo, T. Tél, Vortex flow generated by a magnetic stirrer, Am. J. Phys. 75 (2007)1092-1098.

[35] C.B. Mendive, D. W. Bahnemann, M.A. Blesa, Microscopic characterization of the photocatalytic oxidation of oxalic acid adsorbed onto TiO_2 by FTIR-ATR, Cat. Today 101 (2005) 237-244.

[36] I. Grčić, M. Obradović, D. Vujević, N. Koprivanac, Sono-Fenton oxidation of formic acid/formate ions in an aqueous solution; From an experimental design to the mechanistic modeling, Chem. Eng. J. 164 (2010) 196-207.

[37] A. Chemseddine, H. P. Boehm, A study of the primary step in the photochemical degradation of acetic acid and chloroacetic acids on a TiO_2 photocatalyst, J. Mol. Catal. 60 (1990) 295-311.

[38] L. Davydov, P.G. Smirniotis, Quantification of the Primary Processes in Aqueous Heterogeneous Photocatalysis Using Single-Stage Oxidation Reactions, J. Catal. 191 (2000) 105–115.

[39] A.R. Tôrres, E.B. Azevedo, N.S. Resende, M. Dezotti, A comparison between bulk and supported TiO_2 photocatalysts in the degradation of formic acid, Braz. J. Chem. Eng. 24 (2007) 185-192.

[40] M.A. Nawi, A. H. Jawad, S. Sabar S, W.S. Wan Ngah, Immobilized bilayer TiO_2/chitosan system for the removal of phenol under irradiation by a 45 watt compact fluorescent lamp, Desalination 280 (2011) 288–296.

[41] N. Quici, M.L. Vera, H. Choi, G. Li Puma G, D.D. Dionysiou, M.I. Litter, H. Destaillats, Effect of key parameters on the photocatalytic oxidation of toluene at low concentrations in air under 254 + 185 nm UV irradiation, Appl. Catal. B 95 (2010) 312-319.

[42] A. Turolla, D. Santoro, J.R. de Bruyn, F. Crapulli, M. Antonelli, Nanoparticle scattering characterization and mechanistic modelling of UV-TiO_2 photocatalytic reactors using computational fluid dynamics, Water Res. 88 (2016) 117-126.

[43] A. M. Díez, F. C. Moreira, B. A. Marinho, J.C.A. Espíndola, L. O. Paulista, M.A. Sanromán, M. Pazos, R.A.R. Boaventura, V.J.P. Vilar, A step forward in heterogeneous photocatalysis: Process intensification by using a static mixer as catalyst support, Chem. Eng. J. 343 (2018) 597-606.

Figure captions

Fig.1.Schematics of modeling approach.

Fig.2. Schematics for presentation of plate positions in cylindrical coordinates: (a) characteristic radial distances in PR-A and PR-B and (b) projection of plate lenght to axial coordinate in the reactor space in PR-A.

Fig. 3. The LVRPA profiles in the annular space of PR-A at 254 and 365 nm and PR-B (254 nm only) with different TiO_2 loadings (pH = 4)

Fig. 4. The distribution of the incident photon flux on the surface of TiO_2-chitosan films on a single plate in: (a) PR-A under UVA and (b) UVC irradiation and in (C) PR-B under UVC irradiation. The projection of the profile of the light source over the plate is shown as a thin dotted line. Green lines show the average values of the incident photon flux used in modelling.

Fig. 5. The kinetics of FA and OA photocatalytic degradation over suspended TiO_2 (0.4 g L^{-1}) at pH 4. Single component FA (a) and OA (b) solutions with different initial concentration (all in PR-B under UVC). FA-OA mixture (each 125 mg/L^{-1}) in PR-A under UVA (c) and UVC irradiation (d), and in PR-B under UVC irradiation (e). Experimental data presented by symbols and model results by lines.

Fig.6. Morphology of the surface of the TiO_2-chitosan film by SEM (a); Details of the magnified film surface: cut on the film shows the depth of the top layer (7.10 μm), SEM-EDS mapping analysis of Ti and C revealed the prevalent existance of Ti in the top layer, while C emerged from the bottom layer.

Fig. 7. The kinetics of FA and OA photocatalytic degradation over immobilized TiO_2 – chitosan thin films. FA-OA mixture (each 125 mg/L^{-1}) in (a) PR-A under UVA and (b) UVC irradiation (4 plates) and in PR-B under UVC irradiation using one (c) and two (d) plates. Experimental data presented by dots and model with lines.

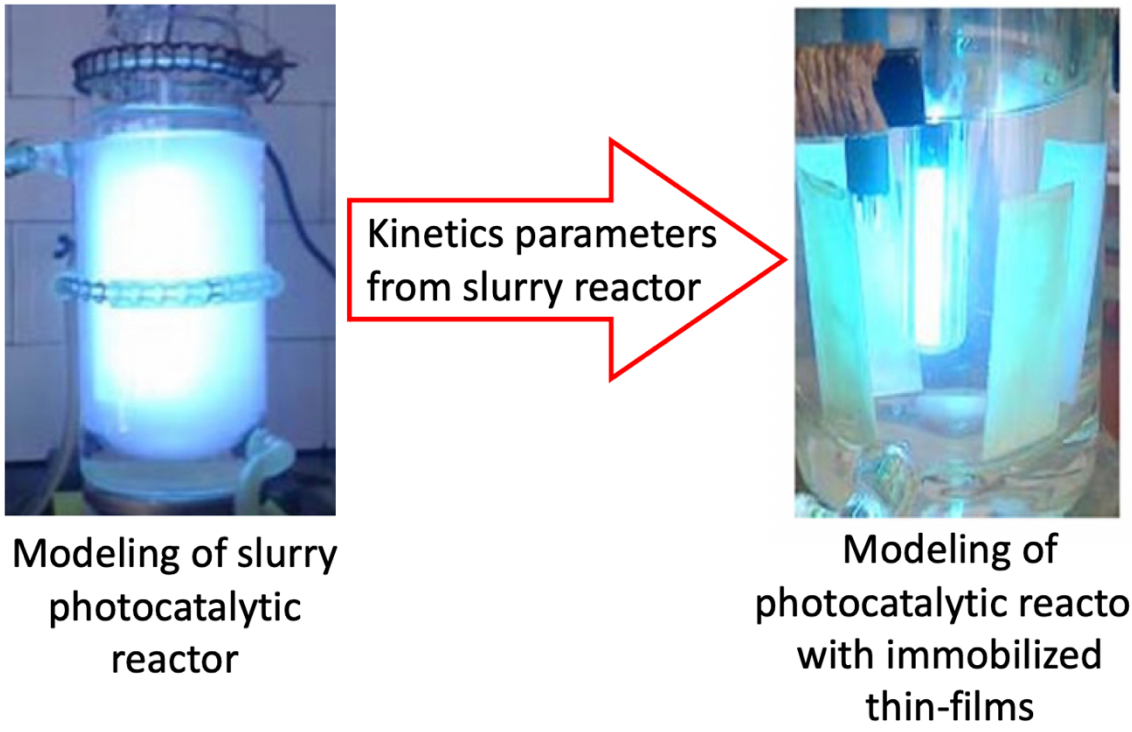
Kinetics parameters
from slurry reactor
Modeling of slurry
photocatalytic
reactor
Modeling of
photocatalytic reactor
with immobilized
thin-films

Fig. 1.

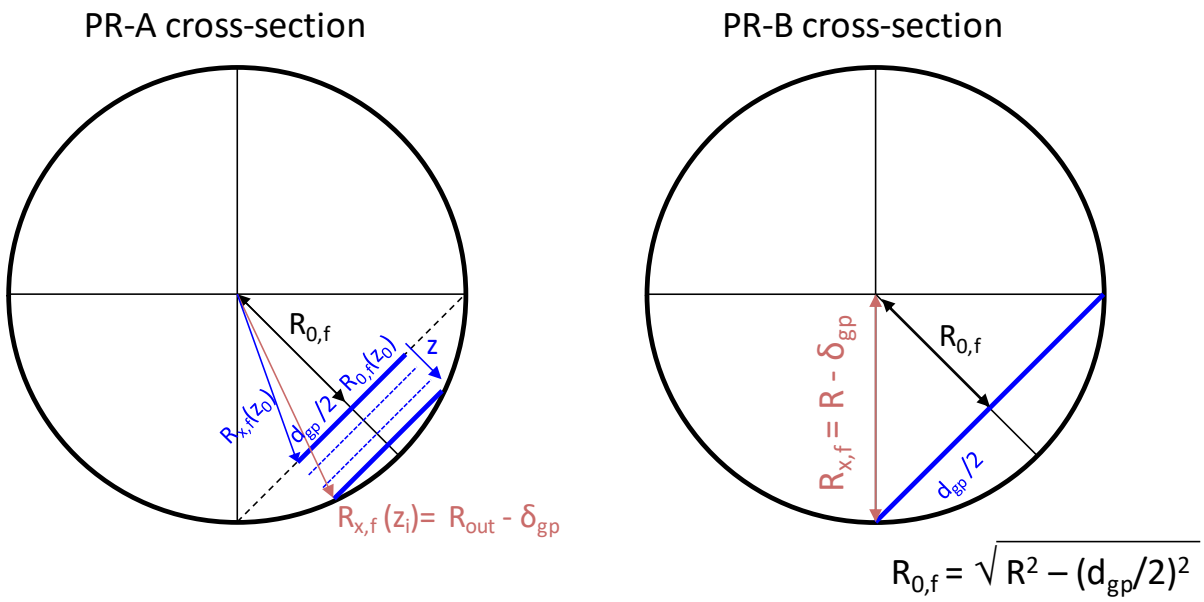
PR-A cross-section
PR-B cross-section
R0,f
R0,f(z0)
z
Rx,f(z0)
dgp/2
Rx,f (zi)= Rout - δgp
Rx,f = R - δgp
R0,f
dgp/2
R0,f = √ R2 – (dgp/2)2

Fig.2a.

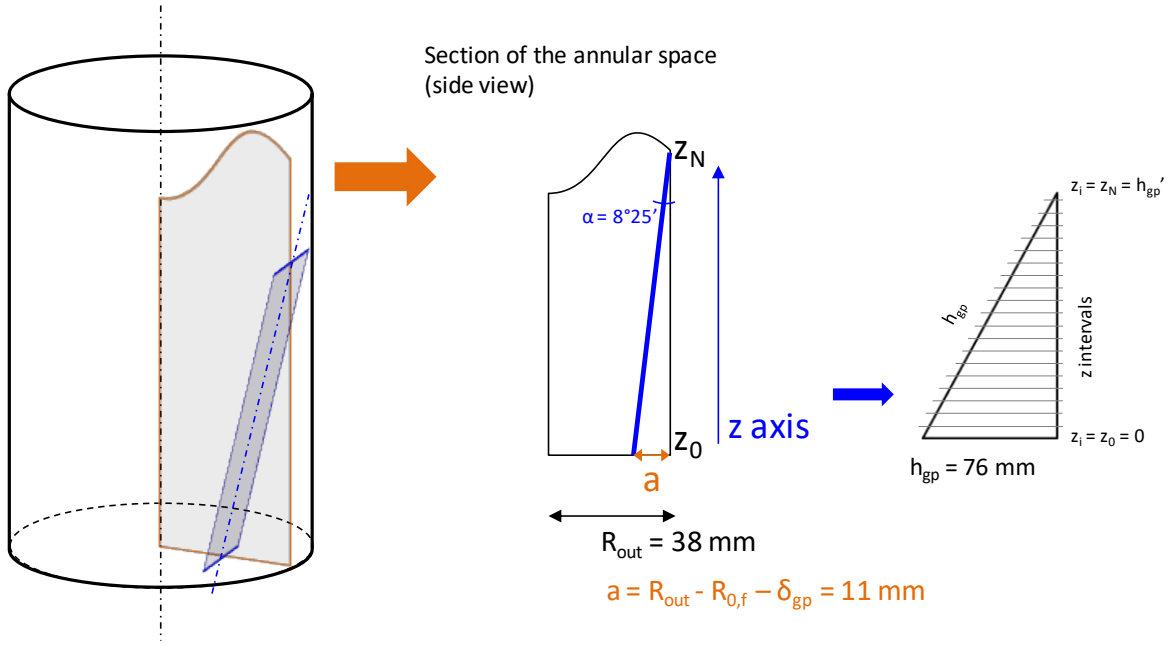
Section of the annular space
(side view)
zN
α = 8°25'
z0
z axis
a
Rout = 38 mm
a = Rout - R0,f – δgp = 11 mm
zi = zN = hgp'
hgp
z intervals
zi = z0 = 0
hgp = 76 mm

Fig.2b.

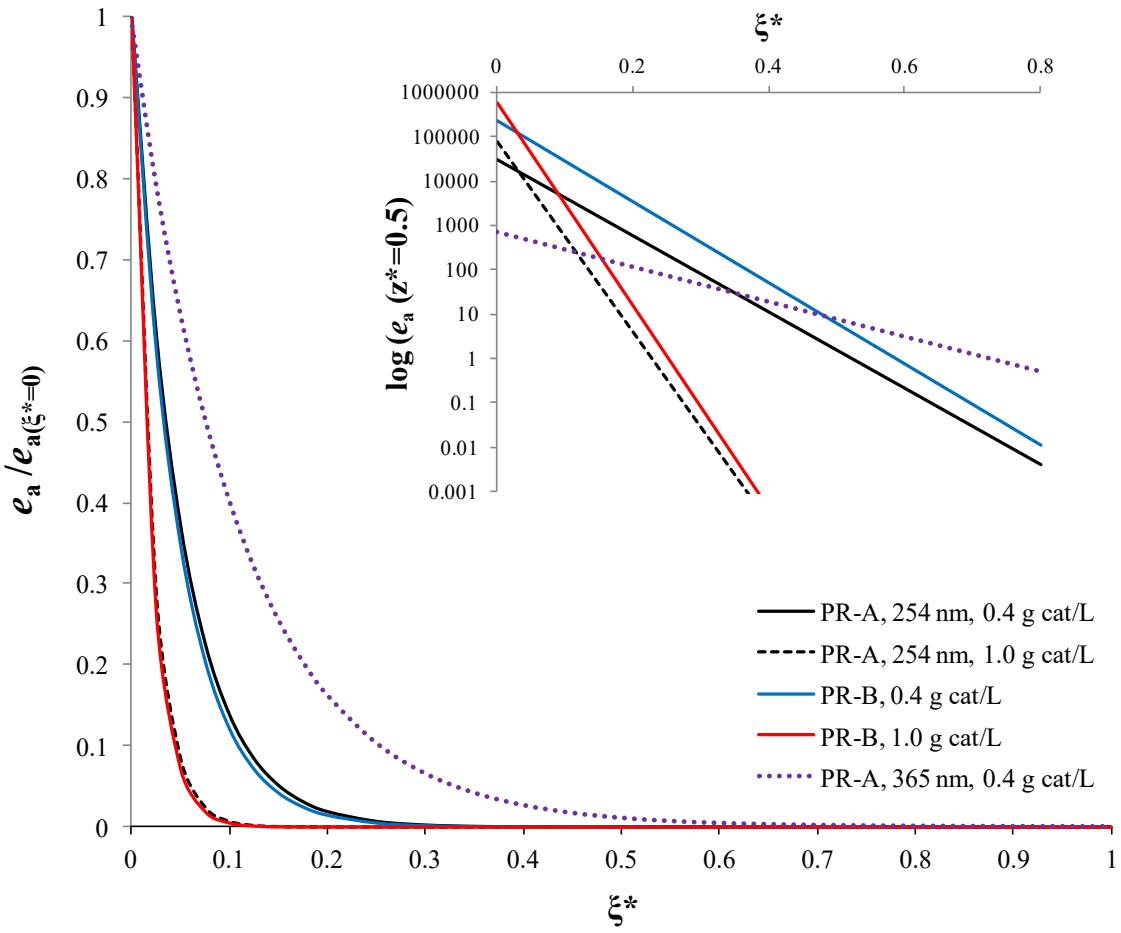
$e_a / e_{a(\xi^*=0)}$
ξ^*
$\log (e_a\ (z^*=0.5)$
PR-A, 254 nm, 0.4 g cat/L
PR-A, 254 nm, 1.0 g cat/L
PR-B, 0.4 g cat/L
PR-B, 1.0 g cat/L
PR-A, 365 nm, 0.4 g cat/L

Fig.3.

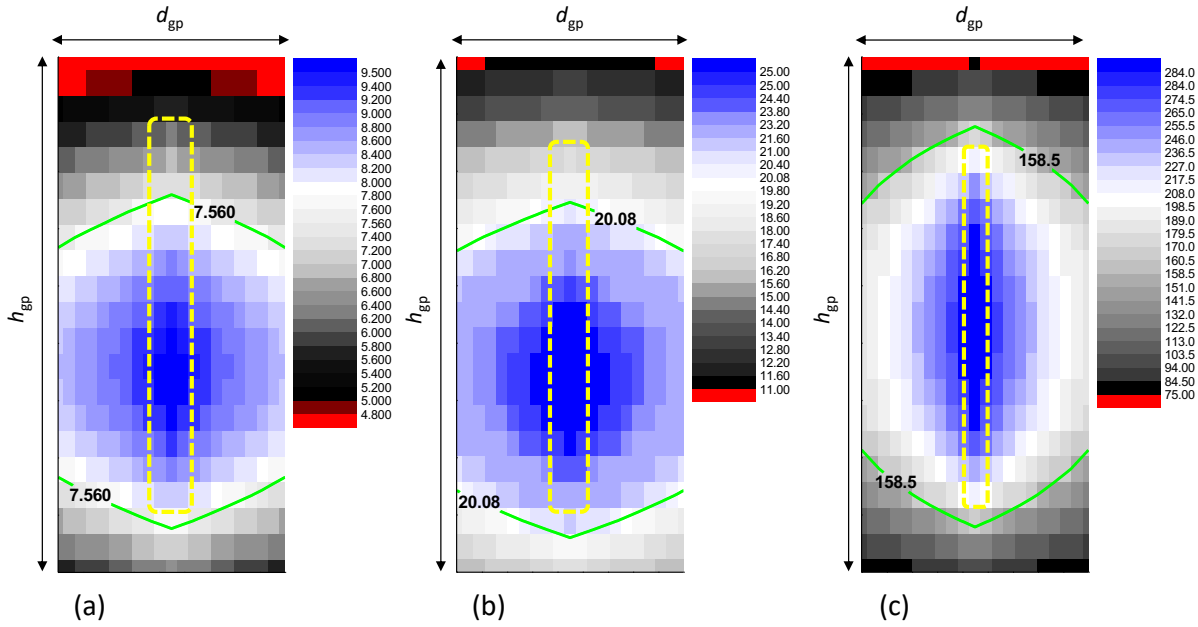
d_{gp}
h_{gp}
7.560
20.08
158.5
(a)
(b)
(c)

Fig.4.

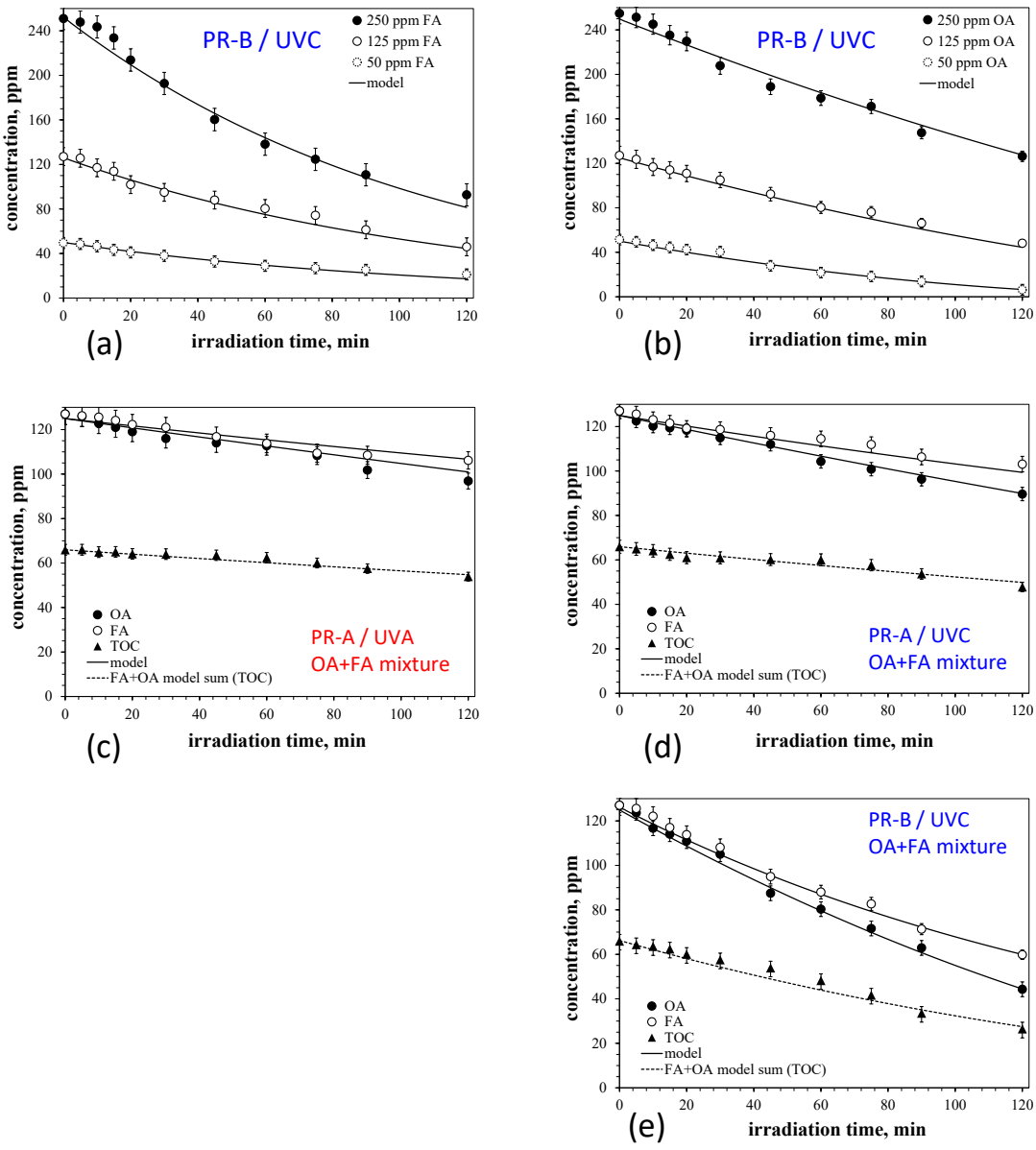
PR-B / UVC
250 ppm FA
125 ppm FA
50 ppm FA
model
concentration, ppm
irradiation time, min
(a)
PR-B / UVC
250 ppm OA
125 ppm OA
50 ppm OA
model
concentration, ppm
irradiation time, min
(b)
OA
FA
TOC
model
FA+OA model sum (TOC)
PR-A / UVA
OA+FA mixture
concentration, ppm
irradiation time, min
(c)
OA
FA
TOC
model
FA+OA model sum (TOC)
PR-A / UVC
OA+FA mixture
concentration, ppm
irradiation time, min
(d)
PR-B / UVC
OA+FA mixture
OA
FA
TOC
model
FA+OA model sum (TOC)
concentration, ppm
irradiation time, min
(e)

Fig. 5.

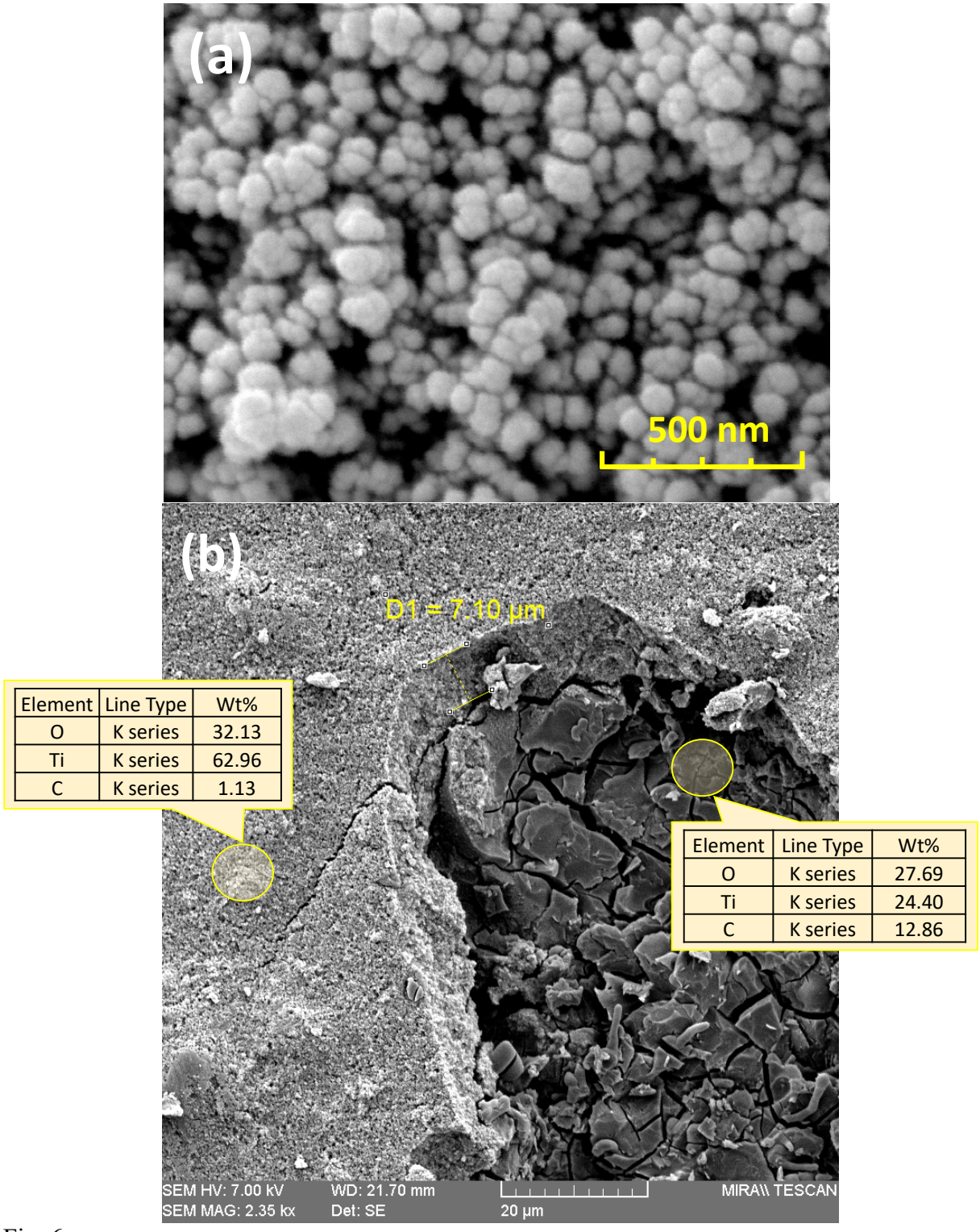
(a)
500 nm
(b)
D1 = 7.10 µm
Element | Line Type | Wt%
O | K series | 32.13
Ti | K series | 62.96
C | K series | 1.13
Element | Line Type | Wt%
O | K series | 27.69
Ti | K series | 24.40
C | K series | 12.86
SEM HV: 7.00 kV
SEM MAG: 2.35 kx
WD: 21.70 mm
Det: SE
20 µm
MIRA\\ TESCAN

Fig. 6.

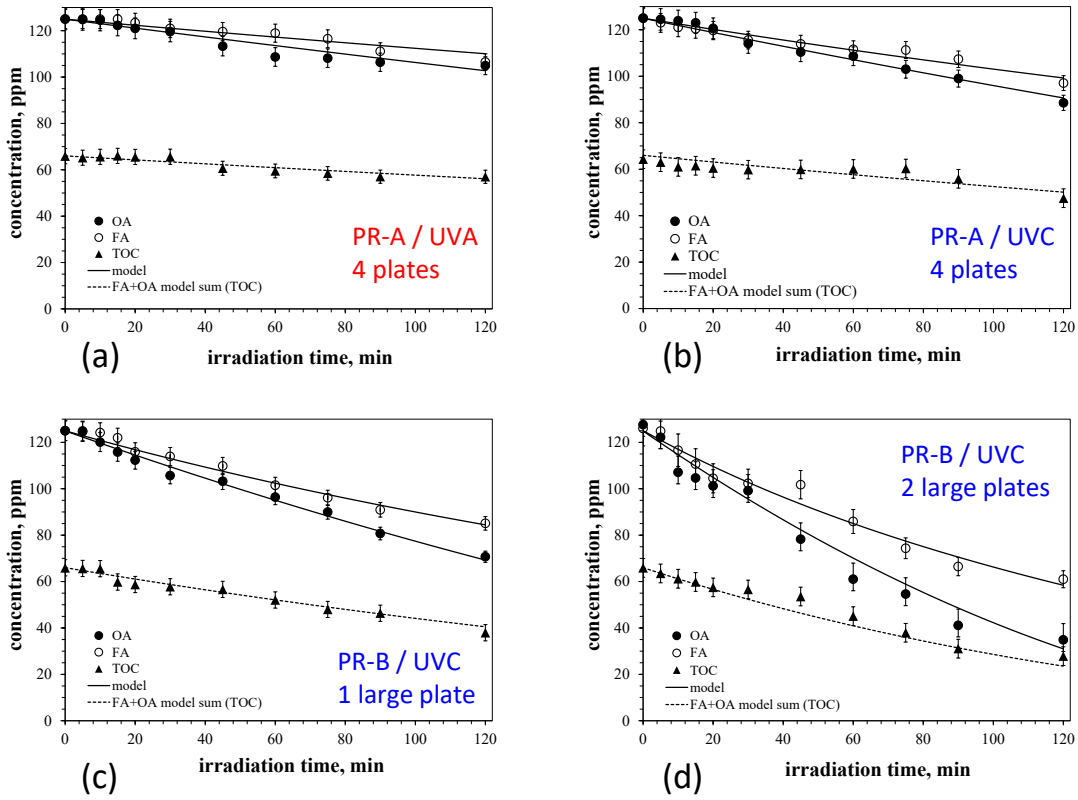
concentration, ppm
irradiation time, min
OA
FA
TOC
model
FA+OA model sum (TOC)
PR-A / UVA
4 plates
(a)
PR-A / UVC
4 plates
(b)
PR-B / UVC
1 large plate
(c)
PR-B / UVC
2 large plates
(d)

Fig. 7.

Table 1 Photoreactors (PR-A and PR-B) and UV lamps characteristics

Reactor	**PR-A**	**PR-B**
Height (H), cm	9.5	22.0
Outer radius (R), cm	3.8	4.5
Inner radius (ηR), cm	0.8	1.2
Volume (V), cm^3	500	1500
Irradiation source	**UVP PenRay lamp 90-0012-01**	**UVP PenRay lamp 90-0019-04**	**UVP PenRay lamp 90-0004-07**
Primary emission output, nm	254	365	254
Lamp length (L), cm	5.38	5.72	15.24
Lamp radius (R_L), cm	0.375	0.475	0.475
Wall Intensity (I_w), W m^{-2}	344.16	84.17	1715.78

Table 2 Lumped values of the volumetric rate of photon absorption in slurry reactors and the incident photon flux on the surface of immobilized photocatalyst

		Slurry suspension		**Immobilized catalyst**
	Irradiation wavelenght (nm)	**TiO_2 concentration (g L^{-1})**	**e^a_{Lump} (W m^{-3})**	**$I_{0,Lump}$ (W m^{-2})**
PR-A				
	254	0.4	1827	20.1
		1.0	2530	
	365	0.4	810	7.6
PR-B	254	0.4	12846	158.5
		1.0	18074	

Table 3 Model parameters of photocatalytic oxidation of OA and FA over slurry suspension and TiO_2-chitosan films.

	UVA	UVC
k_{FA}, kmol $m^{-3/2}$ s^{-1} $W^{-1/2}$	$(7.68 \pm 0.09) \times 10^{-6}$	
$K_{L,FA}$ m^3 $kmol^{-1}$	10.45 ± 0.85	
$k_{OA,A}$, $kmol^{1/2}$ s^{-1} $W^{-1/2}$	$(3.67 \pm 0.34) \times 10^{-8}$	
$k_{OA,B}$, $m^{3/2}$ s^{-1} $W^{-1/2}$	0.56 ± 0.06	
α', m^3 s^{-1} W^{-1}	45.20 ± 2.30	
β', m^3 $kmol^{-1}$	$(1.30 \pm 0.13) \times 10^{-4}$	
μ_{app}, m^{-1}	21.39	163.35 (PR-A) 65.44 (PR-B)
ε	0.26	0.31 (PR-A) 0.25 (PR-B)
$\kappa^*_{app,film}$ [a]	50.5 ± 5.6	321.8 ± 35.8

[a] Calculated for 4 plates in PR-A and 1 plate in PR-B

Supporting Information

Modeling the photocatalytic oxidation of carboxylic acids on aqueous TiO_2 suspensions and on immobilized TiO_2-chitosan thin films in different reactor geometries irradiated by UVA or UVC light sources

Ivana Grčić[1,*], Natalija Koprivanac[2] and Gianluca Li Puma*[3]

[1]Faculty of Geotechnical Engineering, University of Zagreb, Hallerova aleja 7, HR-42000, Varaždin, Croatia

[2]Faculty of Chemical Engineering and Technology, University of Zagreb, Marulićev Trg 19, HR-10000, Zagreb, Croatia

[2]Environmental Nanocatalysis & Photoreaction Engineering, Department of Chemical Engineering, Loughborough University, Loughborough, LE11 3TU, United Kingdom

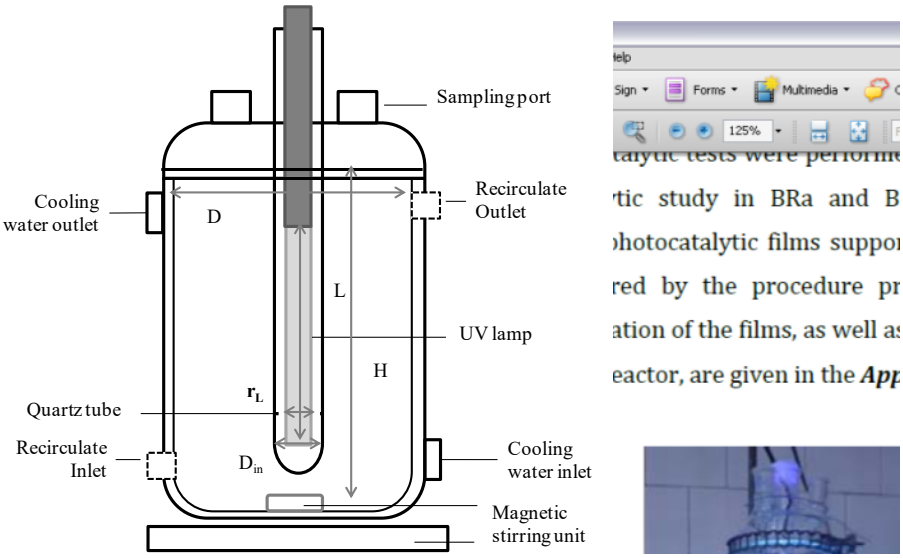

Fig. S1. Schematics of the photoreactor and image of PR-B working in slurry mode.

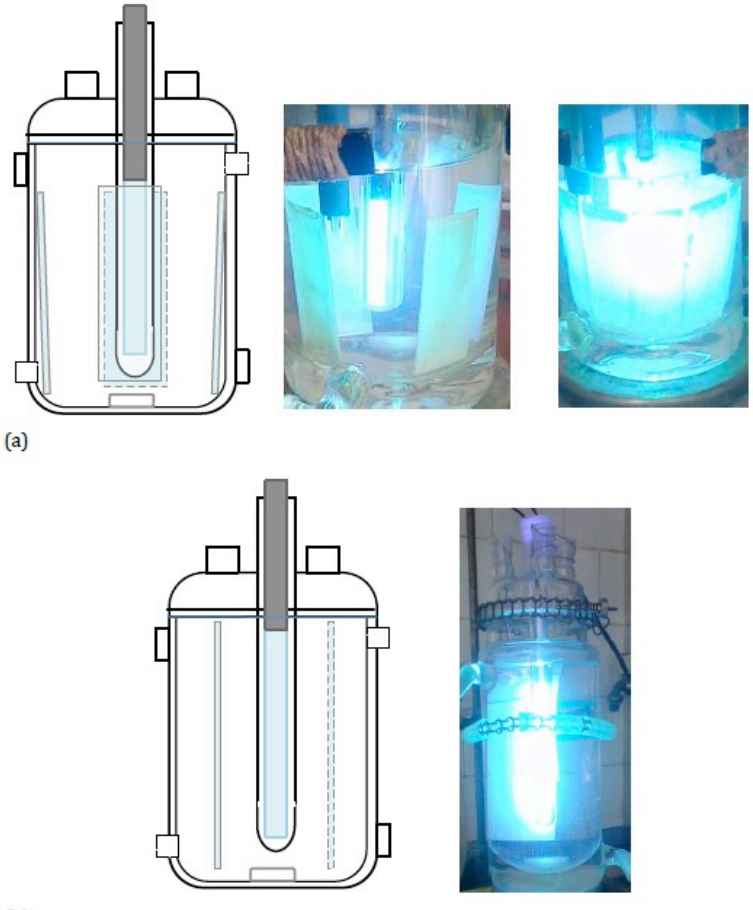

Fig. S2. Arrangement of the photocatalytic plates in the PR-A (a) and PR-B (b) configurations.

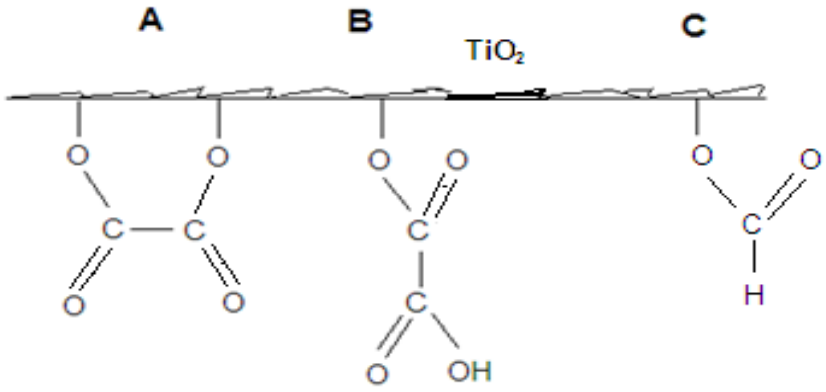

Fig. S3. Surface complexes of OA (A and B) and FA (C) on TiO_2.

1. Reactor hydrodynamics

The flow Reynolds number for magnetic stirring was calculated from literature [11,34]:

$$Re = \frac{\Omega\left(\frac{a}{2}\right)^2}{\upsilon}$$

where Ω and *a* represent the rotational frequency and the length of the magnetic stirrer bar, respectively. Different rotational speeds of the stirrer bar resulted in the different Reynolds numbers and caused different degrees of radial and axial catalyst suspension within the reaction space.

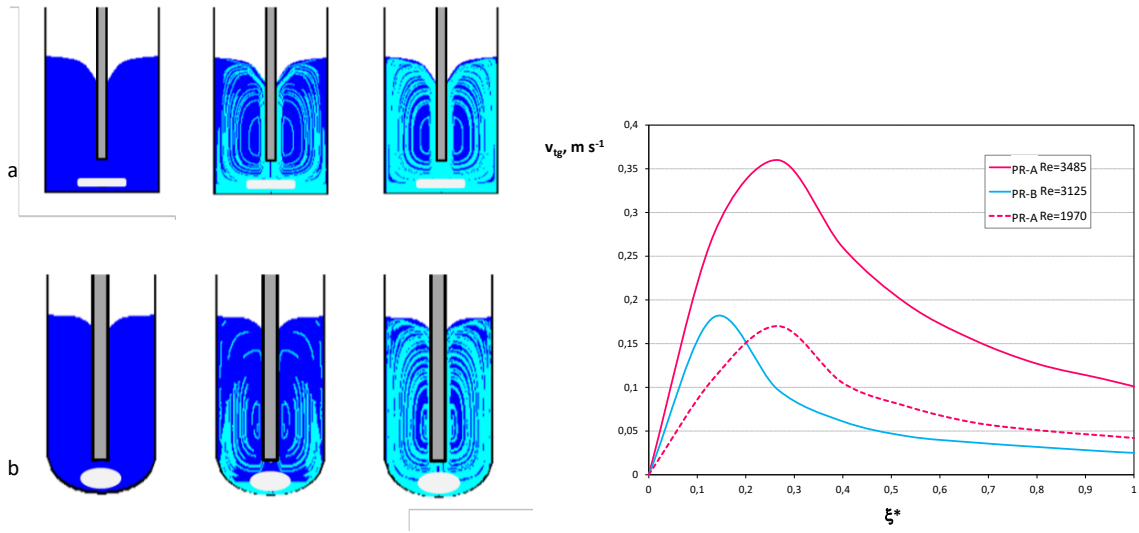

Fig. S4. Approximate flow simulation in the cylindrical reactor with flat, PR-A (a) and eliptical bottom , PR-B (b); gray tube in the middle of the reactor represent the quartz tube for the UV lamp. Radial profile of tangential velocity in photoreactors (c).

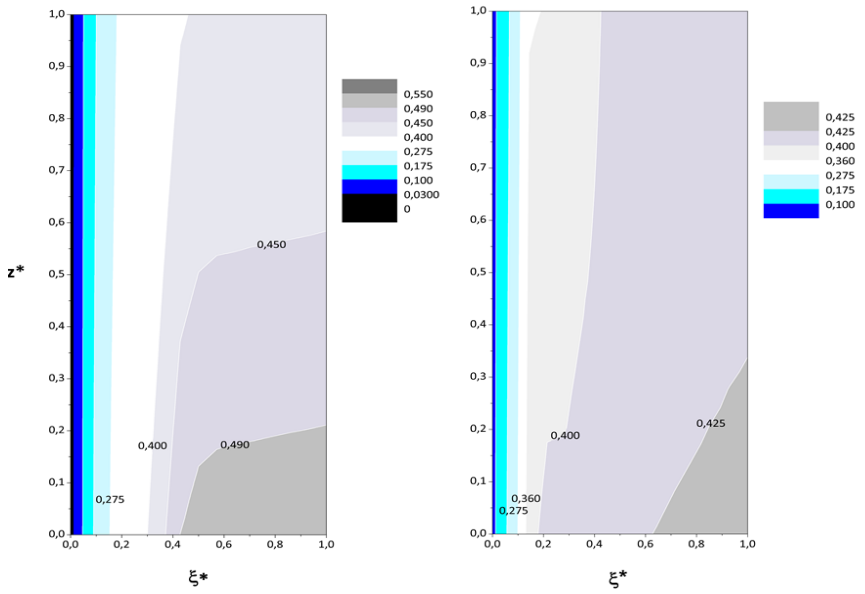

Fig. S5. Local concentration profiles of TiO_2 photocatalysts in the axial cross-sectional area of the PR-A cylindrical reactor loaded with 0.4 g L^{-1} of photocatalyst. Transient regime (Re = 1970) (left) and fully developed turbulent flow (Re = 3485) (right).

Table S1 SFM model parameters.

Parameter	Equation

a	$a = 1 - \omega p_f - \dfrac{4\omega^2 p_s^2}{(1 - \omega p_f - \omega p_b - 2\omega p_s)}$
b	$b = \omega p_b + \dfrac{4\omega^2 p_s^2}{(1 - \omega p_f - \omega p_b - 2\omega p_s)}$
τ	$\tau = (\sigma + \kappa) c_{cat} R(1 - \eta)$
τ_{app}	$\tau_{app} = a\tau\sqrt{1 - \omega_{corr}^2}$
ω	$\omega = \dfrac{\sigma}{\sigma + \kappa}$
ω_{corr}	$\omega_{corr} = \dfrac{b}{a}$
γ	$\gamma = \dfrac{1 - \sqrt{1 - \omega_{corr}^2}}{1 + \sqrt{1 - \omega_{corr}^2}} \exp(-2\tau_{app})$

Table S2 Reaction scheme for the heterogeneous photodecomposition of oxalic acid on TiO_2

Reaction step	
S_0	Activation (common to both pathways) $TiO_2 + h\square \rightarrow h^+ + e^-$
S_1	Adsorption (species A) on dark/illumination conditions $[site]+C_2O_4H^-_{(sol)} \leftrightarrow C_2O_4H^-_{(ads)A}$
S_2	Adsorption (species B) on dark/illumination conditions $[site]+C_2O_4H^-_{(sol)} \leftrightarrow C_2O_4H^-_{(ads)B}$
S_3	Adsorption of oxygen $[site]+O_{2(sol)} \leftrightarrow O_{2(ads)}$
S_4, S_5	Hole trapping (via OH^-) and σ bond rupture (fast kinetics) $(OH^-)_{ads}+h^+ \leftrightarrow OH^\bullet$ $C_2O_4H^-_{(ads)B}+OH^\bullet \rightarrow CO_2H^\bullet_{(ads)B}+CO_2+OH^-$
S_6	Hole trapping (direct) and σ bond rupture (slow kinetics) $C_2O_4H^-_{(ads)A}+h^+ \rightarrow CO_2H^\bullet_{(ads)A}+CO_2$
S_7	Final mineralization (common to both mechanisms) $CO_2H^\bullet_{(ads)}+O_2 \rightarrow O_2H^\bullet+CO_2$
S_8	Electron capture $O_{2(ads)}+ e^- \rightarrow O_2^{\bullet-}$
S_9	Hole–electron recombination $e^-+h^+ \rightarrow$ heat
$S_{10\text{-}12}$	Complementary (assumed fast) reactions $O_2^{\bullet-} + H^+ \rightarrow H_2O^\bullet$ $2O_2H^\bullet \rightarrow H_2O_2+H_2O$ $H_2O_2 \rightarrow H_2O+O_2$

Table S3 Hydrodynamics and solid-liquid mixing properties in a slurry cylindrical reactor PR-A.

Ω, [revolution s^{-1}]	**Hydrodynamics**					**Degree of suspension, %**	
	Re	$v_{tg,max}$, m s^{-1}	$v_{tg,average}$, m s^{-1}	vortex depth, mm	turbulent shear rate in the bulk, s^{-1}	axial	radial
900	3485	0.3640	0.2010	5.4	39.5	24.7	84.1
510	1970	0.0920	0.0524	1.3	18.0	56.6	84.4